Journal of Power Sources 196 (2011) 3659–3663

Contents lists available at ScienceDirect

Journal of Power Sources

journal homepage: www.elsevier.com/locate/jpowsour

Short communication

$LiFe_xMn_{1-x}PO_4$: A cathode for lithium-ion batteries

Jian Hong[a], Feng Wang[b], Xiaoliang Wang[c], Jason Graetz[a,*]

[a] Department of Sustainable Energy Technologies, Brookhaven National Laboratory, Upton, NY 11973, USA
[b] Department of Condensed Matter Physics and Materials Science, Brookhaven National Laboratory, Upton, NY 11973, USA
[c] Center for Functional Nanomaterials, Brookhaven National Laboratory, Upton, NY 11973, USA

ARTICLE INFO

Article history:
Received 8 November 2010
Received in revised form
12 December 2010
Accepted 13 December 2010
Available online 21 December 2010

Keywords:
Cathode
Lithium manganese phosphate
Iron substitution
Nanoporous
Carbon coating

ABSTRACT

The high redox potential of $LiMnPO_4$, ~4.0 vs. (Li^+/Li), and its high theoretical capacity of 170 mAh g^{-1} makes it a promising candidate to replace $LiCoO_2$ as the cathode in Li-ion batteries. However, it has attracted little attention because of its severe kinetic problems during cycling. Introducing iron into crystalline $LiMnPO_4$ generates a solid solution of $LiFe_xMn_{1-x}PO_4$ and increases kinetics; hence, there is much interest in determining the Fe-to-Mn ratio that will optimize electrochemical performance. To this end, we synthesized a series of nanoporous $LiFe_xMn_{1-x}PO_4$ compounds (with $x = 0$, 0.05, 0.1, 0.15, and 0.2), using an inexpensive solid-state reaction. The electrodes were characterized using X-ray diffraction and energy-dispersive spectroscopy to examine their crystal structure and elemental distribution. Scanning-, tunneling-, and transmission-electron microscopy (viz., SEM, STEM, and TEM) were employed to characterize the micromorphology of these materials; the carbon content was analyzed by thermogravimetric analyses (TGAs). We demonstrate that the electrochemical performance of $LiFe_xMn_{1-x}PO_4$ rises continuously with increasing iron content. *In situ* synchrotron studies during cycling revealed a reversible structural change when lithium is inserted and extracted from the crystal structure. Further, introducing 20% iron (e.g., $LiFe_{0.2}Mn_{0.8}PO_4$) resulted in a promising capacity (138 mAh g^{-1} at C/10), comparable to that previously reported for nano-$LiMnPO_4$.

1. Introduction

Since the original study of Padhi et al. lithium transition metal phosphate has been considered a promising cathode material for rechargeable lithium-ion batteries [1]. The inexpensive, inherently non-toxic and stable nature of the olivine structure has led to intensive research and development of these materials over the past 10 years. Previous studies have demonstrated impressive rate capabilities in full batteries with a cathode composed of nano-scale $LiFePO_4$ particles coated with a thin, electronically conductive layer [2,3]. The recent commercialization of $LiFePO_4$ further highlights its importance as a cathode for lithium batteries. However, because of its relatively low working-potential ($LiFePO_4$: 3.5 V (vs. Li^+/Li), $LiCoO_2$: 3.7–4.1 V (vs. Li^+/Li)), batteries made with this material have a lower overall energy density. Currently, much effort is geared towards developing new cathodes exhibiting the positive electrochemical properties of $LiFePO_4$ along with greater energy density.

Here, we investigate the higher voltage $LiMnPO_4$ (~4.0 V vs. Li^+/Li) as a promising alternative to $LiFePO_4$ for the cathode in lithium-ion batteries. $LiMnPO_4$ is isostructural with $LiFePO_4$ (olivine) and lithium ion diffusion occurs along a one-dimensional path parallel to the *c* axis. However, $LiMnPO_4$ performs more poorly than $LiFePO_4$ in lithium-ion batteries, and the utilization of its theoretical energy density is seldom realized, even under mild operating conditions [4].

The generally accepted reason for the low observed capacity and rate performance in $LiMnPO_4$ is the high kinetic barrier due to interface mismatch between $MnPO_4$ and $LiMnPO_4$ from a Jahn-Teller distortion [5]. Several attempts have been made to improve performance [6–11]: such as lowering particle size, controlling particle shape (synthesizing plate-shaped particles to decrease the diffusion path), decreasing the size of the unit cell by iron substitution, and doping/substitutions to increase the kinetics. Currently, nano-scale, iron-substituted $LiMnPO_4$ exhibits the best electrochemical performance [1,12]. However, this electrode typically requires more than 25 wt% carbon as the conducting medium, thereby dramatically decreasing the electrodes tap density and increasing cell volume in the full battery.

Recent results demonstrated an increase in kinetics when some of the Mn ions were replaced with Fe to form the solid solution $LiFe_xMn_{1-x}PO_4$ (e.g., $x = 0.1$) [12]. Yamada et al. have also shown that this type of substitution increases the electrode capacity, which reaches a maximum close to its theoretical value at $x = 0.4$

* Corresponding author. Tel.: +1 631 344 3242; fax: +1 631 344 2359.
E-mail address: graetz@bnl.gov (J. Graetz).

0378-7753/$ – see front matter © 2010 Elsevier B.V. All rights reserved.
doi:10.1016/j.jpowsour.2010.12.045

[13]. At very low Fe concentrations ($x \leq 0.1$) a single plateau (3.9 V) is present in the cycling curve, which indicates that the iron may not be contributing much to the capacity since its redox couple occurs at 3.5 V. At higher Fe concentrations ($x > 0.1$) both plateaus are clearly visible (3.5 V and 3.9 V).

Given the higher potential of the Mn-based phosphate, the energy density is greatest using the least amount of Fe necessary to achieve a high, reversible capacity in the electrode. Currently, the optimal composition of $LiFe_xMn_{1-x}PO_4$ is not well defined since it is not known if a near-theoretical capacity can be achieved at lower Fe concentrations. Here we report the performance of carbon-coated nanoporous $LiFe_xMn_{1-x}PO_4$ materials at low Fe concentrations ($x = 0$, 0.05, 0.1, 0.15, and 0.2). In addition, the nanoporous nature of the material is expected to improve the electrochemical kinetics of the material by increasing its surface area and decreasing the diffusion length of Li^+.

2. Experimental

We synthesized $LiFe_xMn_{1-x}PO_4$ in a conventional solid-state reaction as follows: stoichiometric amounts of lithium carbonate (Li_2CO_3), iron oxalate dihydrogen ($FeC_2O_4{\cdot}2H_2O$), manganese carbonate ($MgCO_3$), ammonium dihydrogen phosphate ($NH_4H_2PO_4$), and citric acid ($C_6H_8O_7$) were mixed in isopropanol ethanol using a planetary ball mill (Fritsch) for 3.5 days. The precursors obtained from this process were dried, and heat-treated at 300 °C for 2 h and subsequently at 600 °C for 5 h.

Powder X-ray diffraction (XRD) patterns were acquired on a Philips XRG 3000 Analytical X-ray Diffractometer to identify the phases present in the as-synthesized material; data were collected from 15° to 65° (2 theta) at 0.6° min^{-1}. Synchrotron powder diffraction experiments were performed on beamline X7B of the National Synchrotron Light Source (NSLS) at Brookhaven National Laboratory (BNL). The lattice parameters were determined via Rietveld refinements of the synchrotron diffraction data, using an olivine structure with a *Pnma* space group.

Particle morphologies were characterized by scanning electron microscopy (SEM, Hitachi S-4800) and transmission electron microscopy (TEM, JEOL 2100F). Energy dispersive spectroscopy (EDS) was employed in the electron microscopes to determine the distribution of the elements. Thermogravimetric analyses (TGAs) were performed to determine the amount (weight percentage) of residual carbon in the electrode.

The electrochemical measurements were made with 2016 coin cells. The electrodes were prepared as follows: the $LiFe_xMn_{1-x}PO_4$ ($x = 0$, 0.05, 0.1, 0.15, and 0.2) samples were mixed with super-P carbon black, and a binder – polyvinylidene difluoride (PVDF) powder, in the weight ratio of 80:13.5:6.5 and mixed in a solution of N-methyl-2-pyrrolidinone (NMP) to form a slurry. The slurry was then spread onto an aluminum foil, using a doctor blade with a space of 100 μm, and thereafter, dried at 80 °C for 1 h in a vacuum oven to remove the NMP. The coated aluminum foil was calendared and punched into 13 mm diameter discs. The electrodes were dried at 100 °C overnight under vacuum. 1.0 M $LiPF_6$ in ethylene carbonate and dimethyl carbonate (50:50 in volume) served as the liquid electrolyte, and a sheet of Celgard 2300 was used as the separator. The $LiFe_xMn_{1-x}PO_4$ sample constituted the working electrode (cathode), with the lithium metal foil as the counter/reference electrode (anode). The assembled $Li/LiFe_xMn_{1-x}PO_4$ cells were cycled between 4.4 and 2.8 V (vs. Li^+/Li) at current densities of 15–750 mAh g^{-1} (assuming 1C = 150 mAh g^{-1}) at room temperature. Structural changes occurring in the electrode during the insertion and extraction of the lithium ions were measured by synchrotron XRD using *in situ* coin cells with a Kapton window.

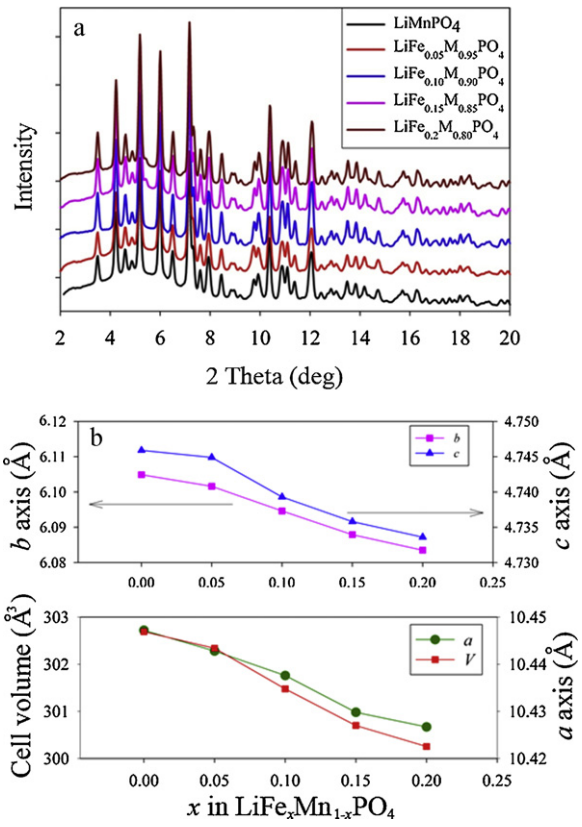

Fig. 1. (a) Synchrotron XRD patterns from $LiFe_xMn_{1-x}PO_4$ ($x = 0$, 0.05, 0.1, 0.15, and 0.2) and (b) the corresponding lattice parameters and unit cell volume.

3. Results and discussion

The as-synthesized powder samples were inspected by synchrotron (Fig. 1a) and Cu Kα (Fig. S1), XRD to confirm the olivine structure. All samples showed a similar diffraction pattern, except for a slight shift towards higher angles with increasing concentrations of iron. Fig. 1b shows the changes in the lattice parameters, and the unit-cell volume as a function of iron content. The unit cell shrinks continuously as iron is introduced into the system. The change is approximately linear, but a slight deviation from Vegard's law is observed at low Fe concentrations (<20%), which is similar to previous results [14]. This is likely due to slight deviations in the homogeneity of the material resulting from the solid-state synthesis. These data confirm that all five materials are single-phase olivine compounds, with an orthorhombic structure. The diffraction data also confirm that the $LiFe_xMn_{1-x}PO_4$ is a true solid solution of $LiMnPO_4$ and $LiFePO_4$. Synchrotron XRD data, acquired for a more detailed structural analysis, was refined (Rietveld refinement) to determine lattice parameters and atomic positions. $LiFe_xMn_{1-x}PO_4$ crystallizes in a *Pnma* space group (orthorhombic) with lattice constants $a = 10.447$ Å, $b = 6.105$ Å, and $c = 4.746$ Å when $x = 0$. Therein, the transition metals (Mn and Fe) occupy *4c* sites, while Li is in a *4a* site. Table 1 compares the cell parameters and Rietveld refinement parameters of $LiFe_xMn_{1-x}PO_4$. Fig. 2 shows the synchrotron powder XRD pattern and the refined pattern from $LiMnPO_4$.

The morphology of the $LiFe_xMn_{1-x}PO_4$ particles was characterized by SEM, high-resolution transmission electron microscopy (HRTEM), and scanning transmission microscopy (STEM). All five samples had a nanoporous structure with particle sizes larger than 1 μm; Fig. 3 shows the SEM images of $LiMnPO_4$ and $LiFe_{0.2}Mn_{0.8}PO_4$. The more detailed SEM images from $LiFe_xMn_{1-x}PO_4$ ($x = 0.05$, 0.1, and 0.15) are shown in Supplementary

Table 1
Lattice parameters for the $LiFe_xMn_{1-x}PO_4$ phases, the instrument error (sigma) is include in brackets.

Iron, y	α (Å)	b (Å)	c (Å)	Volume (Å^3)
$LiMnPO_4$	10.4472(5)	6.1049(3)	4.7459(2)	302.69(3)
$LiFe_{0.05}Mn_{0.95}PO_4$	10.4428(3)	6.1016(7)	4.7449(6)	302.33(6)
Li $Fe_{0.1}Mn_{0.9}PO_4$	10.4376(7)	6.0946(4)	4.7393(3)	301.47(3)
$LiFe_{0.15}Mn_{0.85}PO_4$	10.4298(7)	6.0879(4)	4.7358(3)	300.70(3)
$LiFe_{0.2}Mn_{0.8}PO_4$	10.4267(2)	6.0835(6)	4.7336(5)	300.25(5)

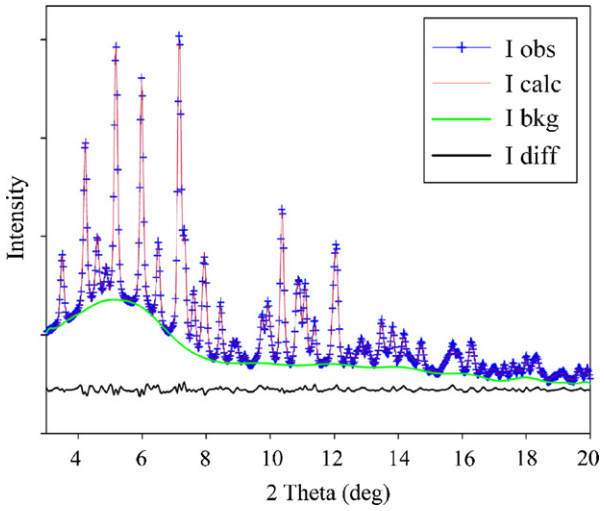

Fig. 2. Synchrotron X-ray diffraction from $LiMnPO_4$ showing the raw data (blue), background fit (green), refined pattern (red) with R_F^2 of 3.43% and the residual (black). (For interpretation of the references to color in this figure legend, the reader is referred to the web version of the article.)

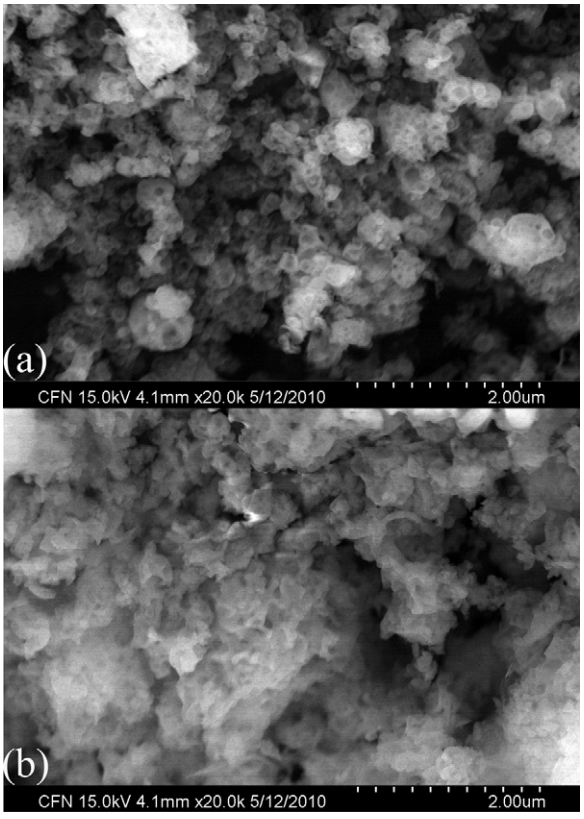

Fig. 3. SEM images from $LiFe_xMn_{1-x}PO_4$ with (a) $x = 0$ and (b) $x = 0.2$ showing mesoporous structural features.

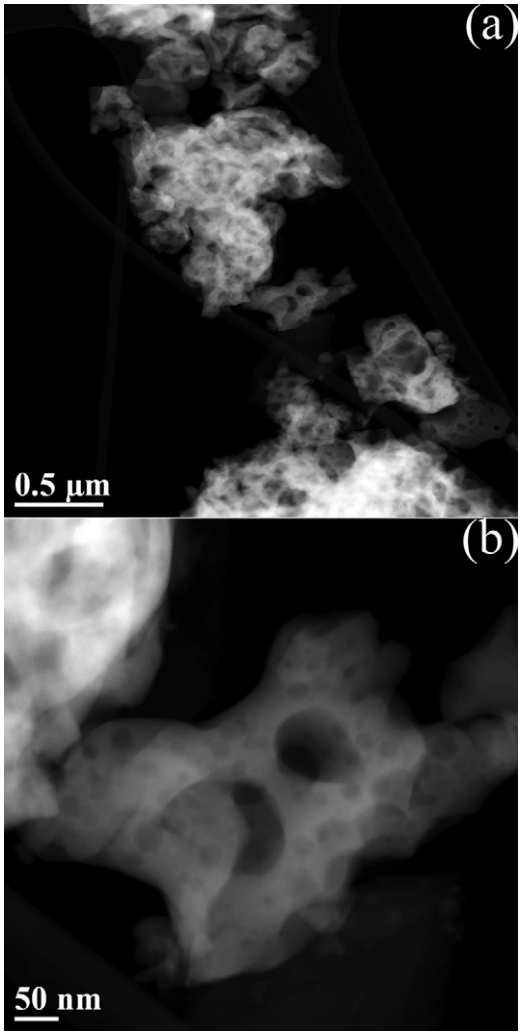

Fig. 4. Annular dark-field TEM images from $LiFe_{0.2}Mn_{0.8}PO_4$ showing the mesoporous features clearly at (a) low and (b) high resolution.

figures (Fig. S2). To inspect the morphology more closely, we checked the detailed topography with STEM, as shown in Fig. 4 for $LiFe_{0.2}Mn_{0.8}PO_4$. The annular dark-field image reveals a nanoporous morphology with the primary particle sizes ranging from ~0.5 μm to 2 μm (Fig. 4a). Fig. 4b gives detailed information on the pores on the particles' surfaces that range from 10 to 100 nm. The nanoporous structure of this material is similar to the material prepared by Dominko et al. [7]. Pore formation is likely from the use of citric acid as the carbon source, and the large quantity of solvent used during grinding. EDS mapping showed that the Fe and Mn ions are uniformly distributed in the particles (Fig. S3).

Fig. 5 shows a HRTEM image of a $LiFe_{0.2}Mn_{0.8}PO_4$ particle covered by a 3-nm thick carbon film. The crystallites have a well-defined orthorhombic symmetry, and the atomic layer is clearly visible. This figure confirms that the crystal structure is well ordered, suggesting an excellent electrochemical performance in a lithium-ion battery. TGA analysis of the as-prepared powder showed that all five samples have approximately 6 weight percent carbon (in the supporting information, Fig. S4). Small differences in weight loss were observed during the TGAs that were independent of iron concentration. These differences were likely due to variations in the rate of gas flow during sintering, or to slight variations in the amount of carbon used in the precursor.

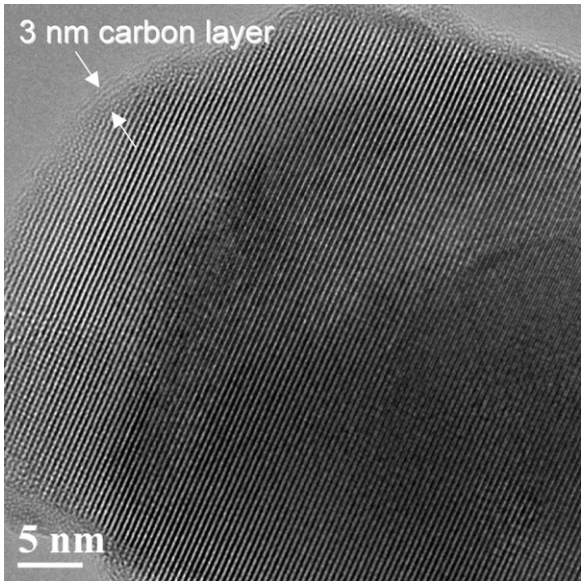

Fig. 5. High-resolution transition electron microscopy image from a particle of $LiFe_{0.2}Mn_{0.8}PO_4$ showing a 3-nm thick carbon surface layer.

Voltage profiles were measured for $LiFe_xMn_{1-x}PO_4$ during galvanostatic discharge at various rates. A single plateau was evident around 4.0 V for $x \leq 0.1$, with a second plateau at 3.6 V for samples with iron concentration greater than 10% ($x > 0.1$). These 4.0 V and 3.6 V plateaus, respectively, are related to the Mn^{3+}/Mn^{2+} and the Fe^{3+}/Fe^{2+} redox couples [15]. Fig. 6a shows the galvanostatic discharge profiles for $LiMnPO_4$ at various rates. This sample ($x = 0$) had a capacity of about 55 mAh g^{-1} when it was discharged with a low current (C/15), and exhibited only 20 mAh g^{-1} at a 2C rate (the C rate was based on a practical capacity of 150 mAh g^{-1}). The capacity of the nanoporous $LiMnPO_4$ was much smaller than that of the nano-scale $LiMnPO_4$ prepared by Wang et al. [12]. However, we note that less carbon was used in our nanoporous electrodes. In addition, the 4.0 V (vs. Li^+/Li) plateau in the voltage, which indicates the redox reaction of Mn^{3+}/Mn^{2+}, is flat in our results.

Iron was incorporated into the material to increase capacity and electrochemical kinetics. At an iron concentration of 15%, the $LiFe_{0.15}Mn_{0.85}PO_4$ electrode exhibited a significant enhancement of capacity up to ~125 mAh g^{-1} at a rate of C/10 (Fig. 6c). At a concentration of 20% iron, the material had a capacity of 130 mAh g^{-1} at C/10 (Fig. 6c). We estimate that the capacity of the active material (not including the carbon) is 133.0 mAh g^{-1} for $LiFe_{0.15}Mn_{0.85}PO_4$, and 138.3 mAh g^{-1} for $LiFe_{0.2}Mn_{0.8}PO_4$ at a rate of C/10. We note that although the capacities achieved with the nanoporous material are similar to those reported for nano-scale $LiMnPO_4$ [12], the nanoporous electrodes were prepared by a much simpler solid-state synthesis reaction. In addition, the nanoporous electrodes require roughly 30% less carbon; with a total of ~18% used (~4.5% resulting from synthesis and 13.5% added during electrode fabrication) compared with 25% carbon in the nano-scale $LiMnPO_4$ [8].

It is well known that during the first cycle, the irreversible capacity is partly due to the formation of the surface–electrolyte interphase (SEI) layer [16]. However, the relationship between the structural changes occurring during cycling and loss of capacity is unknown. Hence, it is of interest to detail the changes in the crystal structure (during cycling) and correlate them with the electrochemical performance for the mixed Fe/Mn metal phosphate [15]; accordingly, we used *in situ* synchrotron XRD to monitor structural changes in these electrodes during cycling. Fig. 7a shows the electrochemical cycling curve and corresponding oxidation state (labeled A–J) at which we acquired the synchrotron XRD ($\lambda = 0.3184$ Å) pattern. Fig. S5a shows the XRD pattern between 4° and 20° in 2θ. The subsequent figures show the same data in more detail over a narrower two-theta range (3–6° (Fig. 7b) and from 8° to 12° in 2θ (Fig. 7c)). The (0 2 0) and (1 2 3) peaks decrease when lithium is inserted into the structure, and return to their original state when lithium is extracted. The only noticeable change after the first cycle is in the (1 2 3) peak at 10.4°, which does not reverse to its original intensity and may indicate a re-orientation of the crystals. Overall, there is no major alteration in crystal structure after the first cycle.

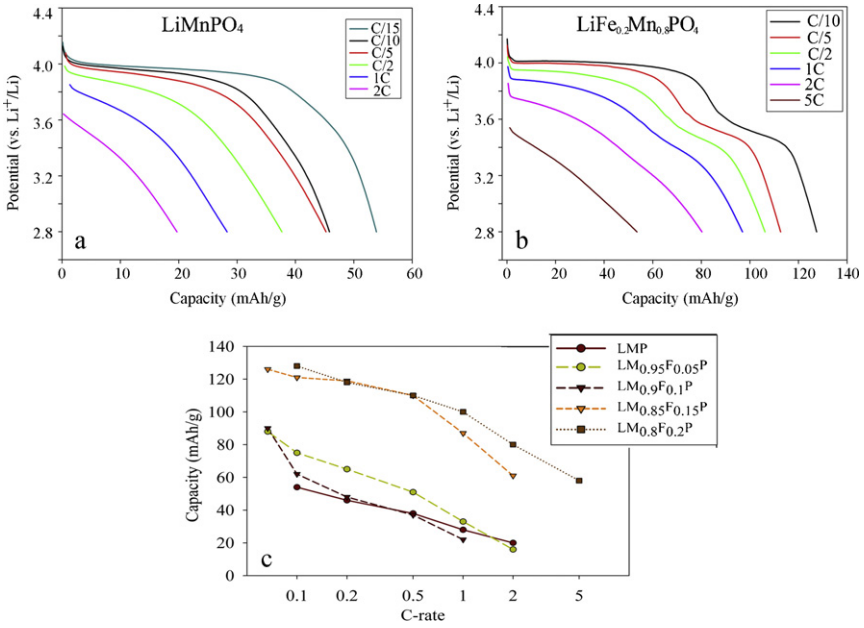

Fig. 6. Electrochemical data showing the C-rate performance for (a) $LiMnPO_4$ and (b) $LiFe_{0.2}Mn_{0.8}PO_4$ along with (c) C-rate test of $LiFe_xMn_{1-x}PO_4$ ($x = 0$, 0.05, 0.1, 0.15, and 0.2).

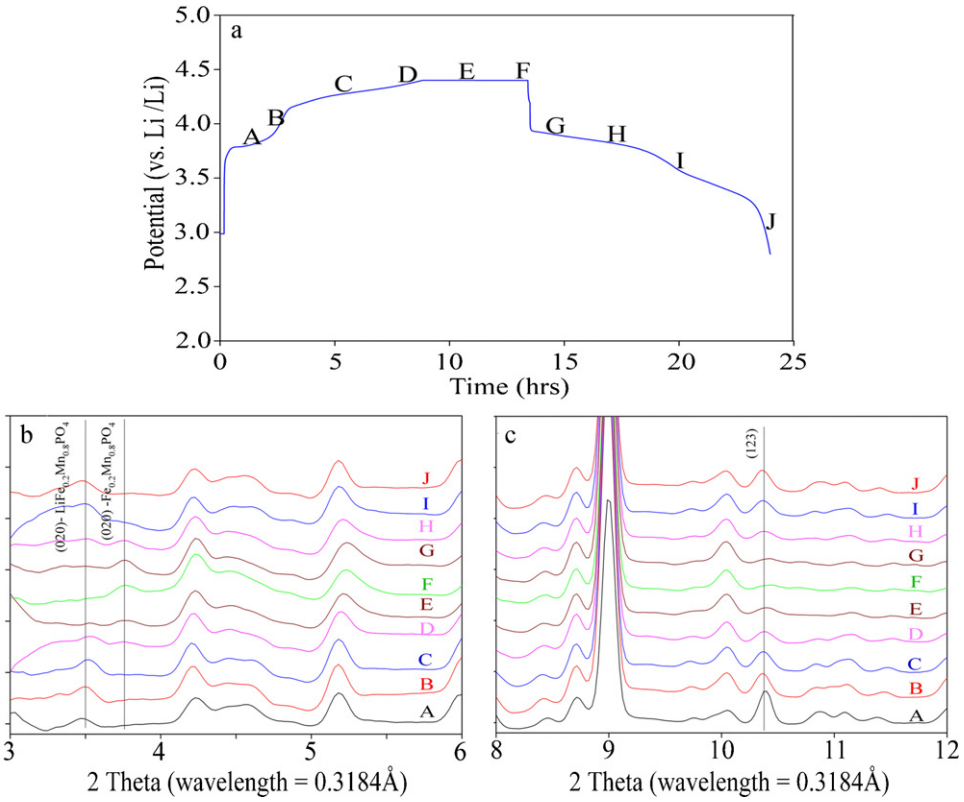

Fig. 7. *In situ* synchrotron XRD analysis of $LiFe_{0.2}Mn_{0.8}PO_4$ showing (a) electrochemical cycling curve and point at which synchrotron XRD pattern was acquired (labeled A–J), (b) synchrotron X-ray 3–6° range in 2θ and (c) synchrotron X-ray 8–12° range in 2θ.

4. Conclusion

We synthesized nanoporous $LiFe_xMn_{1-x}PO_4$ ($x = 0$, 0.05, 0.1, 0.15, 0.2) via a simple solid state reaction and characterized the structure, composition and electrochemical properties. The iron-substituted samples formed a solid solution of $LiFe_xMn_{1-x}PO_4$ and displayed a decreasing unit-cell volume with increasing iron concentration. *In situ* XRD demonstrated that the crystal structure underwent a reversible change when lithium was extracted from, or inserted into the material. Characterization of the morphology by SEM, TEM, and STEM verified the nanoporous structure of all our samples. The electrochemical activity of $LiFe_xMn_{1-x}PO_4$ may be related to this nanoporous morphology and decreased unit-cell volume. The electrochemical tests revealed that the energy density and rate capability of $LiFe_xMn_{1-x}PO_4$ increases with x, while the cell volume of the solid solution simultaneously decreases. Our results demonstrate that when $x = 0.2$, $LiFe_xMn_{1-x}PO_4$ has a capacity of 138.3 mAh g^{-1} at a rate of C/10. Nanoporous $LiFe_{0.2}Mn_{0.8}PO_4$ has an overall energy density comparable to the best performing nano-scale Mn-based phosphates, but can be prepared using an inexpensive solid-state synthesis method. Therefore, we believe nanoporous $LiFe_{0.2}Mn_{0.8}PO_4$ is a promising cathode for lithium ion batteries.

Acknowledgements

The authors thank financial support from the Laboratory Directed Research and Development (LDRD) program under Contract No. DE-AC02-98CH1-886 with the U.S. Department of Energy. The contribution of beamline X7B of National Synchrotron Light Source at Brookhaven National Laboratory is gratefully acknowledged.

Appendix A. Supplementary data

Supplementary data associated with this article can be found, in the online version, at doi:10.1016/j.jpowsour.2010.12.045.

References

[1] A.K. Padhi, K.S. Nanjundaswamy, J.B. Goodenough, J. Electrochem. Soc. 144 (1997) 1188–1194.
[2] B. Kang, G. Ceder, Nature 458 (2009) 190–193.
[3] Y.S. Hu, Y.G. Guo, R. Dominko, M. Gaberscek, J. Jamnik, J. Maier, Adv. Mater. 19 (2007) 1963–1966.
[4] M. Yonemura, A. Yamada, Y. Takei, N. Sonoyama, R. Kanno, J. Electrochem. Soc. 151 (2004) A1352–A1356.
[5] C.A. Burba, R. Frech, J. Power Sources 172 (2007) 870–876.
[6] M. Piana, B.L. Cushing, J.B. Goodenough, N. Penazzi, Solid State Ionics 175 (2004) 233–237.
[7] R. Dominko, M. Bele, M. Gaberscek, M. Remskar, D. Hanzel, J.M. Goupil, S. Pejovnik, J. Jamnik, J. Power Sources 153 (2006) 274–280.
[8] N.H. Kwon, T. Drezen, I. Exnar, I. Teerlinck, M. Isono, M. Graetzel, Electrochem. Solid-State Lett. 9 (2006) A277–A280.
[9] G.Y. Chen, J.D. Wilcox, T.J. Richardson, Electrochem. Solid-State Lett. 11 (2008) A190–A194.
[10] J.S. Yang, J.J. Xu, J. Electrochem. Soc. 153 (2006) A716–A723.
[11] T. Drezen, N.H. Kwon, P. Bowen, I. Teerlinck, M. Isono, I. Exnar, J. Power Sources 174 (2007) 949–953.
[12] D.Y. Wang, H. Buqa, M. Crouzet, G. Deghenghi, T. Drezen, I. Exnar, N.H. Kwon, J.H. Miners, L. Poletto, M. Graetzel, J. Power Sources 189 (2009) 624–628.
[13] A. Yamada, Y. Kudo, K.Y. Liu, J. Electrochem. Soc. 148 (2001) A747–A754.
[14] M. Kopec, A. Yamada, G. Kobayashi, S. Nishimura, R. Kanno, A. Mauger, F. Gendron, C.M. Julien, J. Power Sources 189 (2009) 1154–1163.
[15] K.W. Nam, X.J. Wang, W.S. Yoon, H. Li, X.J. Huang, O. Haas, J.M. Bai, X.Q. Yang, Electrochem. Commun. 11 (2009) 913–916.
[16] J.W. Lee, M.S. Park, B. Anass, J.H. Park, M.S. Paik, S.G. Doo, Electrochim. Acta 55 (2009) 4162–4169.